



Effects of hydrofoil shape and turbine solidity on the wake energy recovery in cross-flow turbines

Stefania Zanforlin¹

Received: 23 September 2021 / Accepted: 23 March 2023 / Published online: 30 April 2023
© The Author(s) 2023

Abstract

Cross-flow turbines (CFTs) are arousing a growing interest to harvest both off-shore wind and tidal currents. A promising characteristic of CFTs could be a high power density in case of multi-device clusters or farms, achievable by shortening the distance between arrays as allowed by the fast energy recovery observed inside the wakes. However just few studies, only concerning symmetrical airfoils/hydrofoils, are found in the literature. By means of 3D Unsteady Reynolds Averaged Navier–Stokes (URANS) simulations and a momentum budget simplified approach, this author investigated the effects of blade profile and turbine solidity on the blade tip vortex generation and then on the mixing mechanisms supporting the reintroduction of streamwise momentum into the wake. Results indicate that: (a) pairs of counter-rotating vortices occurs in the wake, which rotation direction depends on blade profile and it is such as to generate positive vertical advection for camber-out profiles, but negative vertical advection for camber-in profiles; (b) camber-out profiles are much more effective in supporting the wake energy recovery due to the massive vertical advection induced by tip vortices; (c) for camber-in profiles the tip vortices poorly contribute to the wake recovery, that appears delayed and promoted by turbulent transport; (d) higher solidity implies stronger tip vortices and higher turbulent transport, therefore, a faster wake recovery.

Keywords Tidal turbine · Wake recovery · Tip vortex · 3D URANS

1 Introduction

Cross-flow turbines (CFTs) can be considered a valid alternative to horizontal axis turbines (HATs) to harvest the kinetic energies of off-shore wind and tidal currents, thanks to advantageous characteristics: simplicity and therefore low construction costs, ability to work independently of flow direction and, in case of a floating platform sustaining the rotor, more stability in off-shore wind applications, or the possibility of setting generator and gearbox above the sea level in tidal current applications. On the other hand, CFTs are penalized by low starting torque and lower efficiency than HATs. However, the strong point of CFTs compared to HATs, which would more than compensate for the lower efficiency of the single device, is the higher power density achievable in case of a multi-device cluster or farm, i.e. the possibility of

generating a greater amount of electrical energy from a sea limited area. To this end, the devices should be placed tightly by adopting pairs of closely-spaced counter-rotating turbines, that can exploit beneficial fluid dynamic interactions (Dabiri 2011; Zanforlin and Nishino 2016; Ahmadi-Baloutaki et al. 2016; Zanforlin 2018; Brownstein et al. 2019; Su et al. 2021), or by shortening the distances between arrays, as allowed by the fast energy recovery experimentally measured for the first time by Kinzel et al. (2012) in the wakes of a CFT cluster.

To plan efficient layouts for turbine farms, it is of crucial importance to know in depth the energy recovery mechanisms of the wake and to understand which operating and turbine geometrical parameters can support them but, at now, only few studies can be found in literature on this subject. The experimental investigations by Bachant and Wosnik (2015) and Rolin and Porté-Agel (2018) on the 3D character of straight-bladed CFT wakes have shown that the vertical advection induced downstream of the rotor by pairs of counter-rotating vortices occurring at the turbine top and bottom sides plays a dominant role in wake dynamics by entraining high-momentum fluid from the freestream and therefore by supporting an extraordinary wake recovery that

✉ Stefania Zanforlin
stefania.zanforlin@unipi.it

¹ Dipartimento di Ingegneria dell'Energia, dei Sistemi, del Territorio e delle Costruzioni, Scuola di Ingegneria, Università di Pisa, I.go Lucio Lazzarino 1, 56100 Pisa, Italy

makes CFT wakes much shorter than HAT wakes. These vortex pairs are deemed the consequence and evolution of the vortex shedding occurring at the blade tips, although they are visible even in case the blade tips are closed by end-plates, as observed by Ryan et al. (2016), who also tested the role of Tip Speed Ratio (TSR) finding that the strength of the vortex pair increases with TSR, that is defined as:

$$\text{TSR} = \frac{R\Omega}{U_0}$$

where R is the turbine radius, Ω is the angular speed, and U_0 is the freestream velocity. To understand the energy recovery process of the wake in a more comprehensive way, it is possible to combine the direct observation of the main variables of the flow field (velocity and turbulence components) obtainable from experimentation or CFD with an analysis based on the momentum budget approach. One of the first studies of this kind is that carried out by Boudreaux and Dumas (2017) who adopted CFD and the momentum budget analysis to better identifying and quantify the role of advection and turbulent and viscous transport in the wake recovery of the axial-flow and cross-flow turbine concepts. With specific regard to CFTs, the momentum budget analyses can be found in the study of Bachant and Wosnik (2015), Rolin and Porté-Agel (2018), Ouro et al. (2019); Posa (2020) combined Large Eddy Simulation (LES) with the momentum budget, however his study does not allow to consider vertical advection due to the 2.5D nature of the CFD simulations. Some common trends are observable in those studies: in the near wake the dominant mechanisms are vertical (positive contribution) and lateral (negative contribution in the near wake that becomes positive in the medium and far-wake) advections whereas turbulent transport is much less and becomes effective only in the medium-far wake of high-solidity turbines. In the literature there are different definitions of the solidity, σ , in current study it is defined as:

$$\sigma = \frac{Bc}{\pi D},$$

where B is the blade number, c is the blade chord and D is the rotor diameter. However, it should be noted that the aforementioned investigations are concerning symmetrical airfoils/hydrofoils (except for Ryan et al. 2016), and that most of them are turbine high solidities, typical of tidal current applications ($\sigma = 14\%$ in Bachant and Wosnik 2015, 17% in Rolin and Porté-Agel 2018, 32% in Ryan et al. 2016, and 21% in Ouro et al. 2019).

Moreover, as far as the author knows, the only studies in which quantitative comparisons are made of the energy recovery between CFTs of different geometry are those by Villeneuve et al. (2020) and by Villeneuve and Dumas (2021) which are focused, the former, on the effects of end-plates

and, the later, on the effects of tip struts, chordwise position of the blade attachment point, blade pitch angle. Their main findings are that the wake recovery is highly dependent on the very near-wake vortex dynamics, and that any geometric parameter affecting the spatial and the temporal distributions of the blade lift affect the vorticity shed by the blades and therefore can significantly influence the wake recovery of CFTs.

To contribute to achieve a deeper insight on the effects of the turbine geometry on the wake recovery process, in this study qualitative observations of the flow field achieved through 3D URANS simulations are combined with a simplified momentum budget analysis to investigate the influence of blade profile and turbine solidity on the blade tip vortex generation and then on the mixing mechanisms supporting the reintroduction of streamwise momentum into the wake. A hydrokinetic turbine with three straight blades, operating at high Reynolds (typical of both tidal and large-scale wind turbines), is assumed. Two hydrofoils based on NACA0018 are considered: one (in the following, “camber-in”) is obtained by transforming the chord into a circle arc and applying the thickness law to the arc; the other one (in the following, “camber-out”) is obtained by reversing the camber-in one. The camber-in blades are positioned with the camber-line on the circumference of radius R , whereas the camber-out blades have the camber-line tangent to that circumference in correspondence to $\frac{1}{4}$ of the chord (and the chord parallel to the tangent line). Two turbine solidities, $\sigma = 6.34\%$ and 15.9% , are chosen to represent wind and tidal applications, respectively; in the following they are called “low” and “high” solidities since the values are very different, despite for wind applications 6% is considered a moderate to high solidity by many other authors.

2 Methodology

In this section the validation of the 3D numerical model is presented in comparison to experimental data available in literature about velocity profiles in the wake of a CFT. Next, the fundamentals of the momentum budget analysis are recalled, and the details of the much-simplified methodology that has been adopted here to calculate only some of the main terms appearing in the equation are described.

2.1 Set-up and validation of the CFD model

ANSYS-ICEM has been used to generate multi-block structured 3D grids (which means, made up of hexahedral cells only), with the addition of O-grids to thicken the distribution of cells in the areas of greatest interest and at the same time to improve their quality. Two grid levels are used to simulate the blade rotation via the sliding mesh method: a fixed

sub-grid with the outer dimensions of the flow domain and a rotating sub-grid including the turbine blades. All around the blades the grid is very fine to make sure that y^+ at the walls stay below 0.4, following the work of Maître et al. (2013), who analyzed the effect of y^+ realizing that averaged $y^+ > 1$ causes a pressure drag overestimation in turbines exposed to significant flow separation, as happens for high-solidity hydrokinetic turbines. The moving and the fixed domains are joined together by means of a boundary condition (BC) of interface. The other BC are: velocity inlet for the inlet face; pressure outlet for the exit; symmetry for the top boundary; wall for the bottom in case of the validation case study (since it corresponds to the wind-tunnel floor) or symmetry for the main simulations of this paper (since only half turbine is simulated to save computation time).

The simulations are performed using ANSYS-Fluent v19. To model the turbulence, the $k-\omega$ SST (Shear Stress Transport) is adopted (Menter 1994; Wilcox 2008); this model is widely used in the URANS simulation of wind and tidal CFTs since it is considered well appropriate in case of flow characterized by strong adverse pressure as happens in CFTs, especially when operating at low TSR. Several examples can be found in literature showing that a reasonable agreement with wind-tunnel experiments of CFTs is achieved when this model is used (Marsh et al. 2017; Rezaeiha et al. 2019; Hau et al. 2020; Karimian and Abdolahifar 2020). The algorithm for the velocity–pressure coupling is SIMPLEC. About the spatial discretization scheme, the Least Squares Cell-Based (LSCB) is set for gradient; pressure interpolation, turbulent kinetic energy and specific dissipation rate formulations are based on second order schemes. Temporal discretization is also based on a second order implicit method. The convergence criteria for each time-step is 1×10^{-4} for the residuals of continuity, velocity components, turbulence kinetic energy and specific dissipation rate. When using a sliding mesh, to obtain a satisfactory numeric convergence the time-step should not be larger than the time required for advance the mobile interface by a distance corresponding to one cell thus, to consider the smallest cell at the interface, a time-step corresponding to 0.5° of revolution is adopted; this value is also in accordance with Balduzzi et al. (2016).

Since the current paper is focused on the wake dynamics, before to simulate the turbines of interest, the reliability of the overall numerical model has been verified by comparison with the wake experimental data of Vergaerde et al. (2020). These data were chosen because of the very large test section of the wind tunnel that avoid any blockage effect. The turbine has two straight blades with NACA0018 profile, solidity σ of 7%, and aspect ratio (AR) of 1.6:

$$AR = \frac{H}{D}$$

where H is the blade length and D the turbine diameter. The chord-based Reynolds number (Re_c), defined as:

$$Re_c = \frac{\rho \cdot c \cdot R \cdot \Omega}{\mu}$$

is 110000, where ρ and μ are the fluid density and the dynamic viscosity. The freestream velocity (U_0) is 10.7 m/s, and TSR is 3. More details of the experimental apparatus and the operating conditions can be read in Vergaerde et al. (2020).

Some characteristics of the grid adopted for the validation task are depicted in Fig. 1. The fixed domain, which reproduces the real test section, is shown in (a); (b) reveals the cell distribution on the bottom face in the region close the turbine (the interface, in yellow, that separates the fixed part of the domain from the rotating part can be seen); (c) shows a xy scan-plane of the rotating domain, and (d) displays the grid refinement at the blade wall; finally, (e) and (f) show a yz scan-plane of the rotating domain and the grid refinement at the blade wall.

Figure 2 shows horizontal profiles of U/U_0 (where U is the streamwise velocity) achieved with CFD at various x -locations (normalized by D) downstream of the rotor axis; the z -coordinate corresponds to the blade midspan. In Fig. 2a, the sensitivity of results to the revolution number is reported; it can be seen that for the near and medium wake (until $x/D = 6$) it is sufficient to simulate 18 revolutions, whereas at $x/D = 8$ the wake needs at least 21 revs. to be considered completely developed. A sufficient agreement has been found by the comparison between the CFD results (achieved after 18 revs.) and the experimental measurements, as shown in Fig. 2-b.

2.2 Momentum budget approach

The momentum budget approach allows to find the physical mechanisms that mostly favor the wake recovery. At this purpose, the streamwise RANS momentum equation is usually rearranged (Bachant and Wosnik 2015; Boudreaux and Dumas 2017; Ouro et al. 2019), assuming the steadiness and incompressibility for the flow:

$$\begin{aligned} \frac{\partial \bar{U}}{\partial x} = & -\frac{\bar{V}}{\bar{U}} \frac{\partial \bar{U}}{\partial y} - \frac{\bar{W}}{\bar{U}} \frac{\partial \bar{U}}{\partial z} - \frac{1}{\rho \cdot \bar{U}} \frac{\partial \bar{P}}{\partial x} \\ & - \frac{1}{\bar{U}} \frac{\partial}{\partial x} \overline{U'U'} - \frac{1}{\bar{U}} \frac{\partial}{\partial y} \overline{U'V'} \\ & - \frac{1}{\bar{U}} \frac{\partial}{\partial z} \overline{U'W'} + \frac{\nu}{\bar{U}} \left(\frac{\partial^2 \bar{U}}{\partial x^2} + \frac{\partial^2 \bar{U}}{\partial y^2} + \frac{\partial^2 \bar{U}}{\partial z^2} \right) \end{aligned} \quad (1)$$

Equation 1 is time-averaged: all field quantities are decomposed into a time-averaged component and a fluctuating

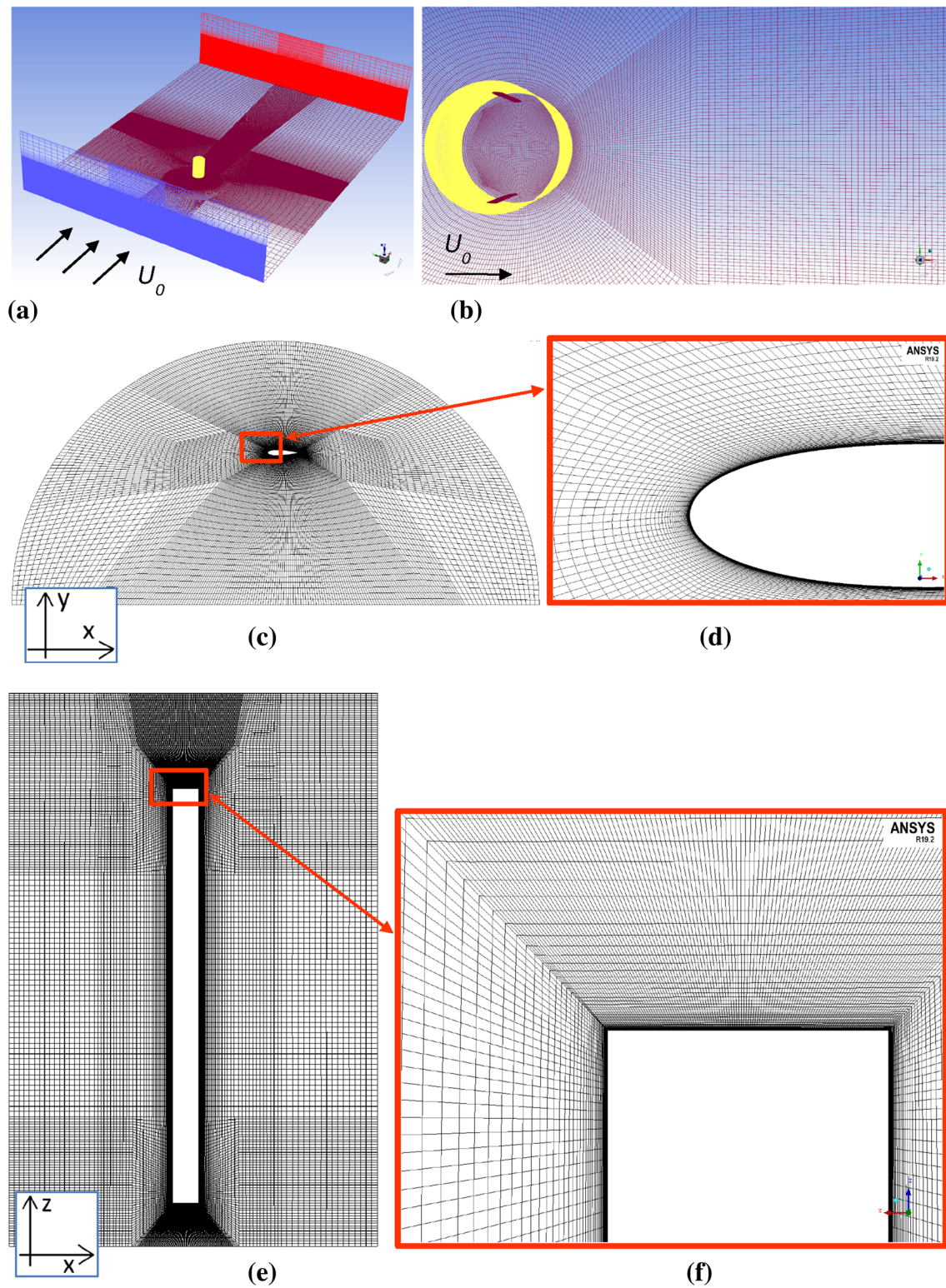


Fig. 1 Grid details for the validation task: **a** inlet (blue), bottom (maroon), exit (red) of the fixed grid, and interface with the rotating sub-grid (yellow); **b** bottom of the fixed grid, the two blades of the turbine, and the sliding interface; **c** xy scan-plane of the rotating domain,

and **d** grid refinement at the blade wall; **e** yz scan-plane of the rotating domain, and **f** grid refinement at the blade wall

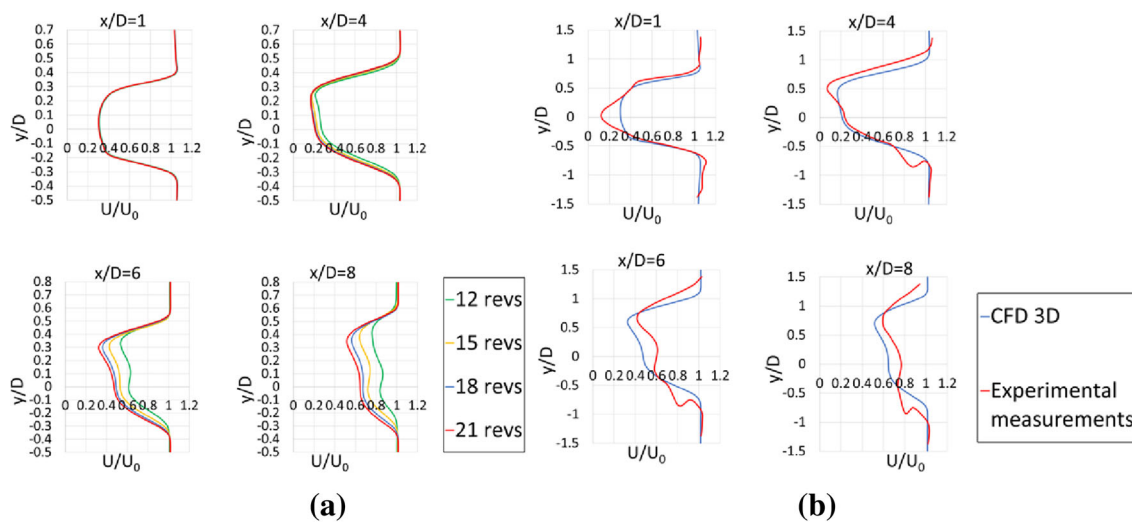


Fig. 2 Streamwise velocity profiles achieved by CFD at different x-locations: **a** effect of the revolution number; **b** comparison with experimental data from Vergaerde et al. (2020)

Table 1 Terms used to compute contributions to streamwise momentum recovery

y advection	$-\overline{V} \cdot \overline{U} \cdot (\partial \overline{U} / \partial y)$
z advection	$-\overline{W} \cdot \overline{U} \cdot (\partial \overline{U} / \partial z)$
Pressure transport	$-(1/\rho \cdot \overline{P}) \cdot (\partial \overline{P} / \partial x)$
x turbulent transport	$-1/\overline{U} \cdot (\partial \overline{U} \overline{U}' / \partial x)$
y turbulent transport	$-1/\overline{U} \cdot (\partial \overline{U} \overline{V}' / \partial y)$
z turbulent transport	$-1/\overline{U} \cdot (\partial \overline{U} \overline{W}' / \partial z)$
Viscous diffusion	$\nu/\overline{U} \cdot (\partial^2 \overline{U} / \partial x^2 + \partial^2 \overline{U} / \partial y^2 + \partial^2 \overline{U} / \partial z^2)$

component, respectively denoted by an overline and a prime symbol. Here it was decided to carry out the time-average calculations on a period of time which corresponds to two revolutions of the turbine. As done in Boudreaus and Dumas (2017), the term on the left-hand side of Eq. 1, that is the streamwise component of the mean streamwise velocity gradient, will be referred in the following as the “wake recovery rate”. The physical meaning of all terms on the right hand of Eq. 1 is specified in Table 1: lateral and vertical advection, streamwise pressure gradient, three terms of turbulent transport (x, y and z derivatives of the Reynolds stresses), viscous diffusion.

It should be observed that a first advantage of CFD is the possibility to calculate all the terms appearing in Eq. 1, whereas in experimental tests this would be technically difficult or very expensive. For instance, the contributions of the streamwise pressure gradient and the streamwise turbulent transport were not computed by Bachant and Wosnik (2015) and Ouro et al. (2019) due to the objective difficulty to obtain

gradients; furthermore, in Bachant and Wosnik (2015) the contribution of streamwise derivative of the viscous stresses was not computed, while in Ouro et al. (2019) the viscous diffusion was considered negligible and then it was omitted. Another advantage of CFD is to be able to use very small computation cells, which leads to finer resolution than experimental work for the terms in Eq. 1. The grid adopted in the current study in the wake region, starting from 2D downstream of the turbine axis and up to the domain outlet, is made of regular parallelepiped cells with uniform spacing in the three directions equal to: 0.43c, 0.35c and 0.28c along x, y and z respectively. To make a comparison, the data were taken on cross-sectional planes with resolution of 0.71c along y and 0.93c along z in Bachant and Wosnik (2015), and 1.17c along y and 0.68c along z in Ouro et al. (2019).

It is good practice to normalize all terms in Eq. 1 by multiplying them by D/U_0 . Moreover, to analyze the evolution of the behavior of the mean wake the terms are spatially averaged over crosswise planes placed at various distances downstream of the rotor; in doing so, not the whole plane is considered but only a portion deemed significant to describe the characteristics of the turbine wake. In the literature there is no unanimity in the choice of the plane portion, since some scientists (Villeneuve and Dumas 2021) adopt the plane part cut by the projection of the frontal area of the turbine whereas others (Posa 2020; Posa and Broglia 2021) prefer the part cut by the iso-contour of the streamwise velocity magnitude corresponding to U_0 . In the current paper the latter approach is followed as in this way only and exactly the region of the wake is considered (i.e. where the fluid velocity is lower than U_0) regardless of whether the wake moves or changes shape. Using angle brackets to indicate a spatial-averaged variable,

Eq. 1 becomes:

$$\begin{aligned} \frac{D}{U_0} \left\langle \frac{\partial \bar{U}}{\partial x} \right\rangle &= \frac{D}{U_0} \left\langle -\frac{1}{\bar{U}} \left(\bar{V} \frac{\partial \bar{U}}{\partial y} \right) \right\rangle + \frac{D}{U_0} \left\langle -\frac{1}{\bar{U}} \left(\bar{W} \frac{\partial \bar{U}}{\partial z} \right) \right\rangle \\ &+ \frac{D}{U_0} \left\langle -\frac{1}{\bar{U} \cdot \rho} \left(\frac{\partial \bar{P}}{\partial x} \right) \right\rangle + \frac{D}{U_0} \left\langle -\frac{1}{\bar{U}} \left(\frac{\partial \overline{U'U'}}{\partial x} \right) \right\rangle \\ &+ \frac{D}{U_0} \left\langle -\frac{1}{\bar{U}} \left(\frac{\partial \overline{U'V'}}{\partial x} \right) \right\rangle + \frac{D}{U_0} \left\langle -\frac{1}{\bar{U}} \left(\frac{\partial \overline{U'W'}}{\partial x} \right) \right\rangle \\ &+ \frac{D}{U_0} \left\langle -\frac{\nu}{\bar{U}} \left(\frac{\partial^2 \bar{U}}{\partial x^2} + \frac{\partial^2 \bar{U}}{\partial y^2} + \frac{\partial^2 \bar{U}}{\partial z^2} \right) \right\rangle \quad (2) \end{aligned}$$

In the current study the momentum budget analysis is very simplified, indeed it is limited to the calculation of the left-hand side of Eq. 2 (i.e., the “wake recovery rate”) and only to the main terms at the right-hand side, which are the vertical and the lateral advections. By doing so, it was possible to use the flow field results provided directly by ANSYS-Fluent, avoiding the need to implement specific but complicated User Defined Functions. In addition to this practical consideration, there are two reasons for this simplification. The first is that if, as in this study, one is interested in carrying out a comparative analysis between turbines of different geometry, the pressure transport term in Eq. 2 is of little interest since the literature shows that its contribution to the wake energy recovery is always negative (since inside the wake the pressure rises progressively until it reaches the freestream value) regardless of the turbine type. The second reason is that, again based on literature, the contribution of viscous diffusion is completely negligible respect to the convection terms. However, in general, the turbulent transport term should not be neglected; to make up for the impossibility of obtaining it directly from the code, a comparative analysis was carried out between the different turbine geometries, based on the calculation of the turbulent kinetic energy and the RMS of the velocity components.

3 Results

The section begins with a paragraph focused on the vortices generated at the blade tips. It will be show that the tip vortex strength depends on blade angular position, hydrofoil profile and turbine solidity, and that the characteristics of the large-scale rotating structures occurring in the turbine wake are determined by those of the tip vortices. Afterwards, the wake momentum replenishment will be analyzed on cross-sectional planes set along the wake, first qualitatively by observing the flow field velocity, then quantitatively by calculating spatial averages for the terms appearing on the streamwise momentum budget equation.

Before starting to analyze the results, a concise overview of the grids and operating conditions is given. Four hydrokinetic CFTs with three straight blades were investigated. They differ for the solidity ($\sigma = 6.34\%$ and 15.9% , called “low” and “high” solidity) and for the cambering of the blade profile (“camber-in” and “camber-out”, as previously defined). The turbines have the same diameter ($D = 6$ m) and aspect ratio ($AR = 2$) but since the solidity is different also the chord and the optimal *TSR* are different. The chord-based Reynolds number (Re_c) is 2.0×10^6 in case of low solidity and 4.2×10^6 in case of high solidity; the operating *TSR* is 1.6 for high solidity, and 2.75 for low solidity; U_0 is 1.75 m/s.

A xy scan-plane of the rotating domain at the blade midspan is visible in Fig. 3, together to the blade walls just go give a schematic of the low and high-solidity turbines considered here. The domain dimensions can be considered “infinite” (i.e., without any wall effect) since they are large: $12D$ upstream and $24D$ downstream of the rotor in streamwise direction (x -axis); $24D$ in crosswise and in vertical directions. To limit the cell number, half turbine is simulated. Doing this, the rotating and the fixed domains have about 9.5×10^6 and 2.6×10^6 hexahedral cells, respectively. To assume sufficiently stable the results at least at $6D$ downstream of the turbine axis, 20 revolutions have been simulated. For further distances the wake is considered not completely developed and then the results are discarded.

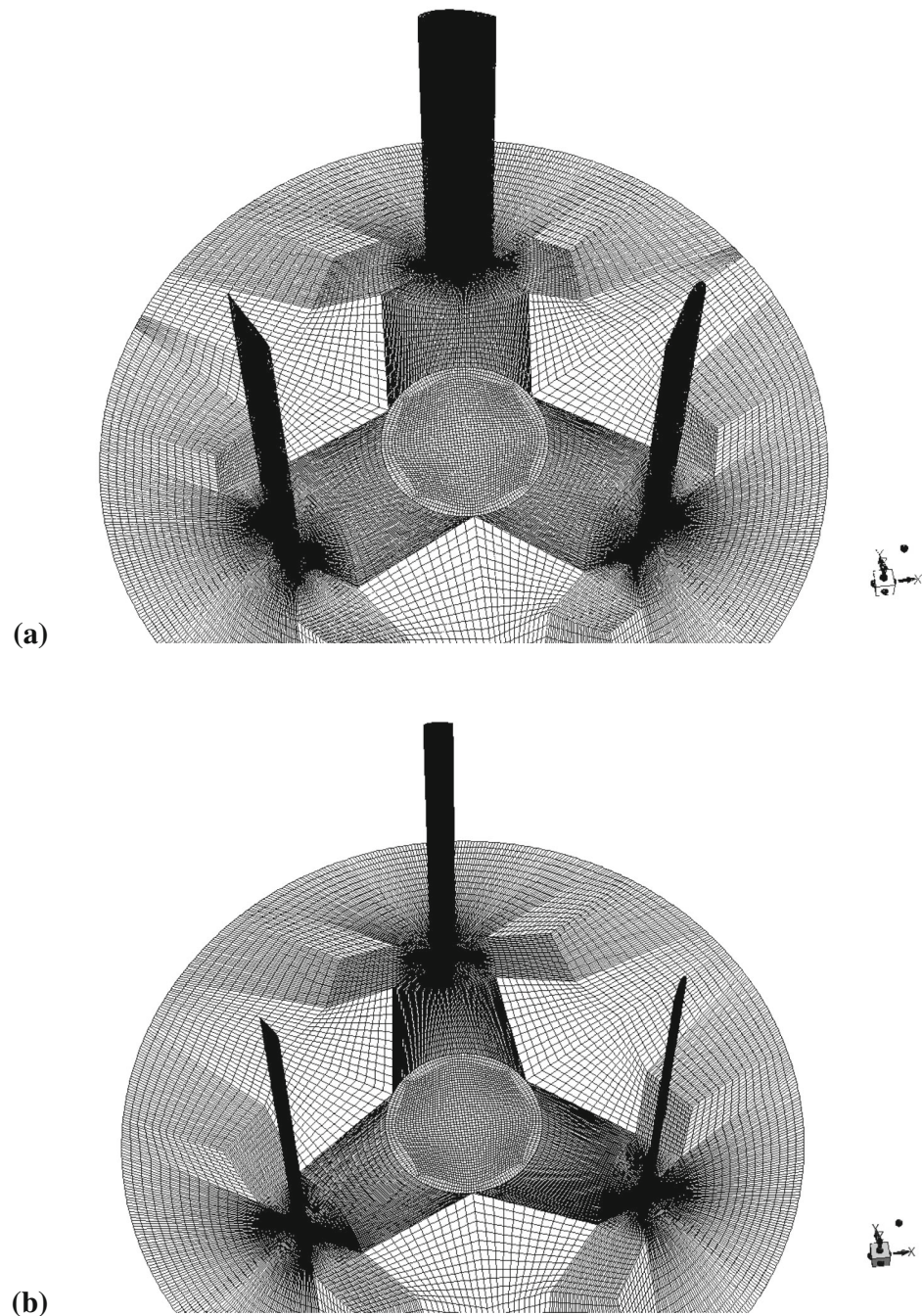
3.1 Origin and evolution of the vortices at the blade tips

Before analyzing the flow fields, some definitions should be recalled. Figure 4a indicates the origin of the blade angular position (θ), and the “upwind” and “downwind” paths. Moreover, it will be practical to name “windward side” and “leeward side” of the wake the sides behind the windward ($\theta = -90^\circ \div 90^\circ$) and the leeward ($\theta = 90^\circ \div 270^\circ$) passage of the blade, respectively (Fig. 4c).

Experimental literature evidenced large-scale coherent structures in the CFT wakes (Bachant and Wosnik 2015; Rolin and Porté-Agel 2018; Ryan et al. 2016; Ouro et al. 2019; Wei et al. 2021). Araya et al. (2017) provided evidence of three typical regions: (i) near wake, governed by periodic blade vortex shedding; (ii) transitional wake, in which the shear-layer generated between the low-velocity wake and the freestream by-pass flow became unstable; and (iii) far-wake, governed by bluff body-like wake oscillations. The current analysis focuses on (i) in this paragraph and, with further details, on (i) and (ii) in the next paragraphs. Whereas, (iii) is out of the observation field, as it is limited to $6D$.

Three kind of vorticities are released by a CFT blade, two of which are z -directed and then also visible in 2D-CFD simulations. The first is the skin friction vorticity occurring inside the boundary layer surrounding a body immersed in

Fig. 3 xy scan-plane of the rotating domain at the blade midspan: **a** high-solidity camber-in turbine; **b** low-solidity camber-in turbine



a fluid in motion. The second is the dynamic stall periodic vorticity, and its intensity and release timing depend on TSR: at low TSR the flow separation is significant long before reaching the maximum attack angle, therefore the vortex is released during upwind; at TSR above the pick performance the flow is little separated and then a weak vortex is released only at the upwind end (i.e., when the suction and pressure sides of the blade reverse each other). However, it should be observed that these z -vorticities play a negligible role in the wake recovery dynamics, as proved by the fact that 2D CFD

wakes appear much longer and poorly re-energized than 3D CFD wakes.

The third type of vorticity is related to tip vortices, a fluid dynamic loss that consists in flow circulation over the tip occurring at the ends of any streamlined body (wings, turbine blades) because of a pressure difference between the two sides of the body. Tip vortex intensity is strong where the pressure difference is high, i.e.: at θ corresponding to great incoming-flow velocity and attack angle, therefore during

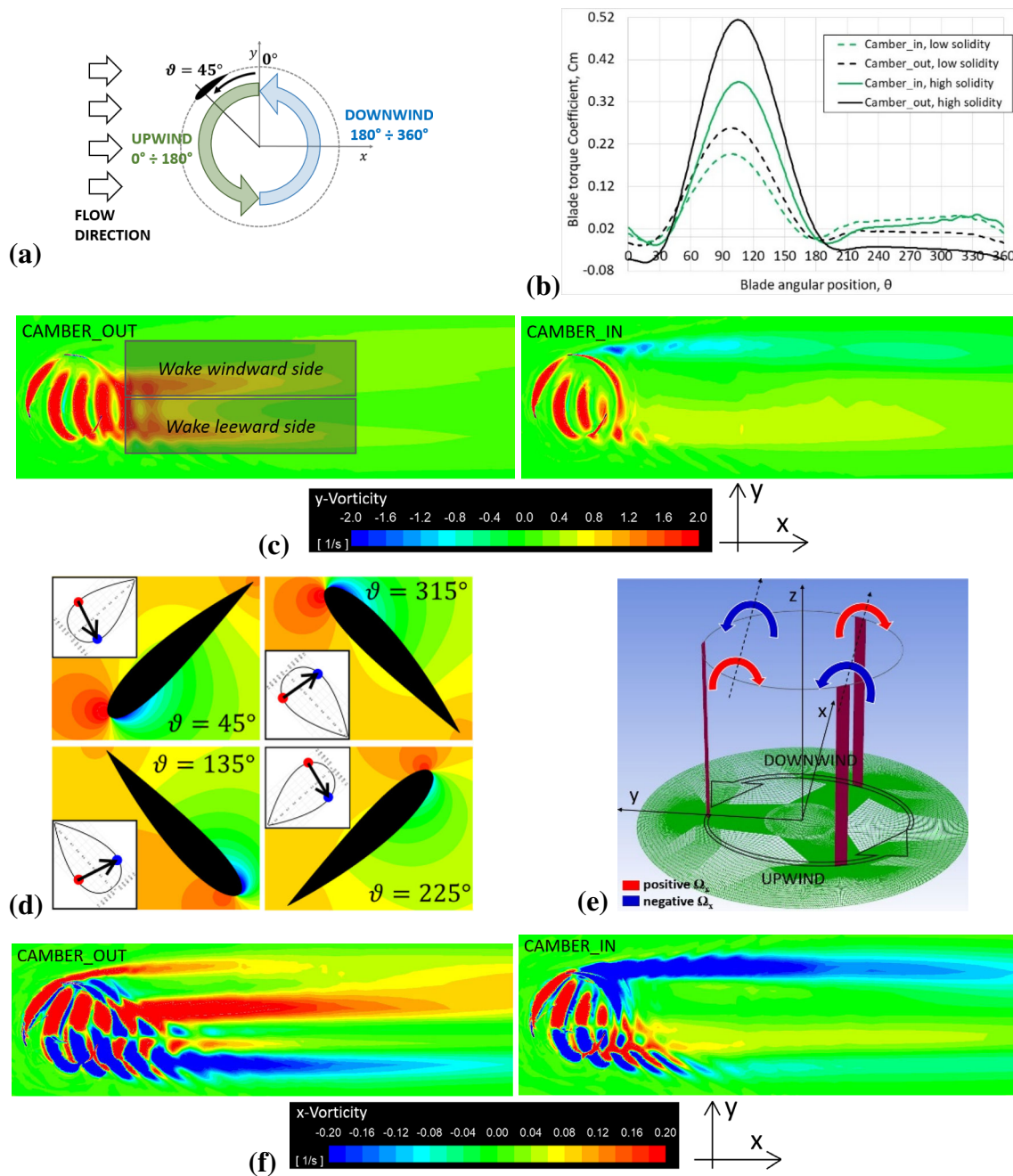


Fig. 4 **a** Definitions of θ , upwind and downwind paths; **b** blade instantaneous torque coefficient for the four turbines of interest; **c** y -vorticity on a plane at $z = H/2$ for the low σ turbines; **d** midspan pressure maps

for four θ values in case of the low σ and camber-in turbine; **e** schematic of the x -rotation direction in each of the 4 quadrants; **f** x -vorticity on a plane at $z = H/2$ for the low σ turbines

central upwind and, in a less extent, central downwind (Zanforlin and Deluca 2018). This it means that where the torque is greater the strongest tip vortices also occur, as also argued by Villeneuve et al. (2020) and by Villeneuve and Dumas (2021). Just as the airfoil shape influences torque distribution, it also affects the strength of the tip vortices released at

a certain θ . As shown in Fig. 4b, in comparison to the camber-out blade, the camber-in blade generates lower torque during upwind and higher torque during downwind, as also found by Qin et al. (2012). Results of Fig. 4b suggest that: camber-out profiles imply strong tip vortices but only in upwind, whereas camber-in generate significant tip vortices also in downwind; extended blade surfaces (high solidity) generate

greater torque in upwind but are also expected to cause higher circulation flowrate over the tips, therefore stronger tip vortices (in upwind).

Not only the intensity but also the spatial orientation of the rotation axis of tip vortices has important consequences on the large-scale motions in near wake. The major component of the tip vorticity is the y -component, that is depicted in Fig. 4c on a horizontal plane located at the height of the blade tips ($z = 6$ m) for the low- σ turbines (here the blades are at $\theta = 0^\circ, 120^\circ$ and 240°). It can be seen that y -vorticity is only positive, which is intuitive, and during upwind it is more intense for the camber-out profile than for the camber-in, as previously justified. The x component is much smaller than the y (in the current calculations it resulted from half to one order of magnitude lower) and its positive or negative direction varies with the angular position of the blade. To understand the dependence of the rotation direction from θ , it is useful to divide the blade path into four quadrants (two for the upwind path, and two for downwind path) and analyze the static pressure field around the blade when this is about in the middle of each quadrant (in Fig. 4d the following values of θ were chosen as representative of the four quadrants: $45^\circ, 135^\circ, 225^\circ$ and 315°). The positions on the blade profile for the center of the overpressures acting on the pressure-side and for the center of the low pressures acting on the suction-side were calculated, then the two centers were joined with an arrow, as visible on the small figures in overlay. Since the flow passes over the blade driven by the pressure difference, it is plausible to assume that the direction of motion is roughly represented by the arrow. It follows that the sign of the x -vorticity will be positive for the first part of upwind and downwind, and negative for the second part of upwind and downwind, as schematised in Fig. 4e). It is worth noting that the direction of the arrows differs little from that perpendicular to the blade chord, and that consequently the direction of the x -vorticity only depends on the quadrant, regardless of the airfoil type. However, it must be underlined that in general the extension of the quadrants is not uniform (90° each). Indeed, in the cases that were examined the upwind x -vorticity was positive up to $\theta = 110^\circ$, therefore the quadrant corresponding to the first part of upwind was wider than the quadrant corresponding to the second part. This, together with the fact that the peak of the blade torque occurs at 105° (Fig. 4b), could justify the higher absolute values of the x -vorticity on the windward side of the wake respect to the leeward side.

The vortices generated at the blade tips are advected downstream of the turbine by the freestream, those generated in upwind will interact with those generated in downwind, the weakest will disappear because of viscosity (or will be disrupted by vortices with opposite rotation direction) while only the strongest will still be observable in the wake. Figure 4f) shows the x -vorticity on the horizontal plane at z

$= 6$ m in case of the low-solidity turbines. It can be observed that the strongest tip vortices generated during the blade rotation persist in the near wake. They are, for camber-out blade: the positive vortices generated during the first half of upwind, on the wake windward side; the negative vortices generated during the second half of upwind, on the wake leeward side. For camber-in blade: the negative vortices generated in the second half of downwind, on the wake windward side; a mix of negative and positive vortices generated, respectively, in the second half of upwind and in the first half of downwind, on the wake leeward side.

Finally, it should be pointed out that the aforementioned division of the blade path in four quadrants is a simplification since, to be more precise, the extension of the first quadrant is more than 90° as proved by the fact that in Fig. 4f the x -vorticity released by the blade at $\theta = 120^\circ$ is still red, and this also implies that the second quadrant is much less wide than 90° .

3.2 Wake development and recovery: qualitative observations of the flow field

The effect of the blade profile on the wake recovery is impressively exemplified in Fig. 5, depicting the time-averaged velocity vectors projected on the vertical plane $y = 0$ (i.e., the plane passing through the turbine axis) for the high-solidity turbines. Yellow lines indicate the x -positions corresponding to $1D, 2.5D, 4D$ and $6D$ downstream of the turbine axis. It can be seen that camber-out blades allow a much faster replenishment of the velocity deficit region than camber-in blades. Despite a single vertical view is not sufficient to capture the 3D features of the wake, this figure suggests the occurrence of very different mechanisms of momentum recovery that are attributable only to the blade shape, since this is the only difference between the two turbines.

To recognize these mechanisms, it is useful to analyze the wake evolution on transversal planes placed at $1D, 2.5D, 4D$ and $6D$ from the rotor axis as depicted in Figs. 6, 7 and 8, showing the crosswise velocity vectors and the streamwise velocity maps that have been time-averaged over the last two revolutions. The overlay added rectangular frame indicates the frontal size of the (half, for symmetry) turbine, moreover it must be specified that the observer is located upstream the turbine, therefore the windward side of the wake is on the left and the leeward side is on the right (coherently to the axes reported in the figures). In this study the “wake” is defined as the region characterized by a velocity deficit respect to U_0 , therefore the region colored by blue, green and yellow. U_0 corresponds to the orange, whereas the red region surrounding the wake indicates the high-momentum by-pass freestream which presence is crucial for the gradual replenishment of the wake streamwise momentum.

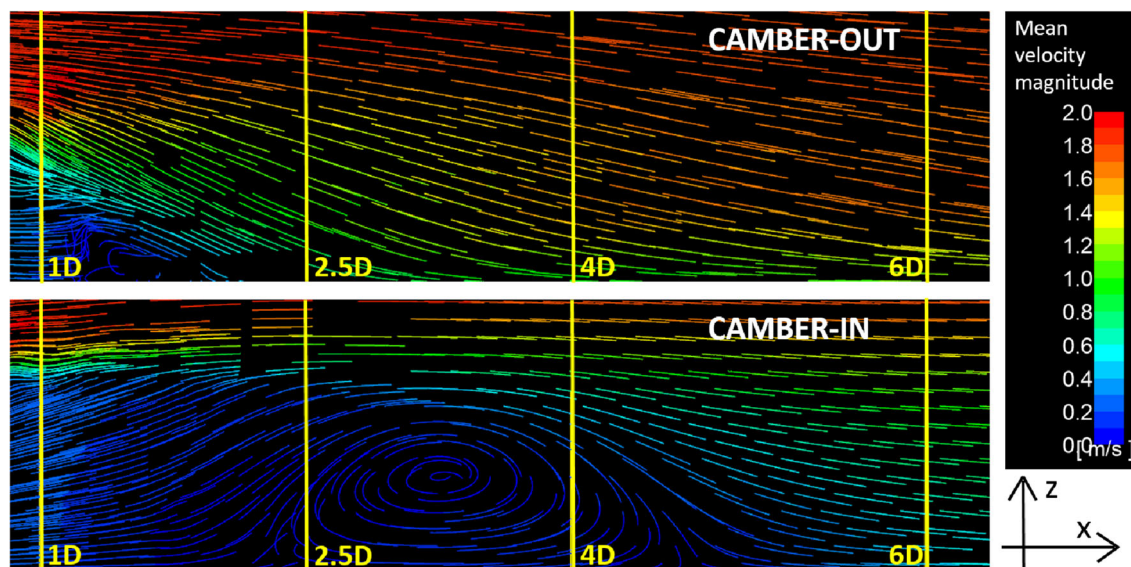


Fig. 5 Time-averaged streamlines on the vertical plane $y = 0$ for the high-solidity camber-out (top) and camber-in (bottom) turbines; yellow lines indicate some x -positions downstream of the turbine axis

Let's start the analysis with the high-solidity case and camber-out blades: a pair of counter-rotating vortices is visible at $x = 1D$; the rotation direction of each vortex is the same observed in Fig. 4e and f, and it is coherent with the tip vortices generated during the upwind passage of the blades; the rotation directions are such as to induce a massive vertical advection which reintroduces momentum into the top of the wake (visible at $x = 2.5D$); since the vortex on the windward side of the wake is much larger and stronger than the one on the leeward side, the energy recovery is asymmetrical and mostly located at the upper-leeward corner of the wake. Similar features were also found by Bachant and Wosnik (2015) and Rolin and Porté-Agel (2018) in case of symmetrical airfoils and solidities close to the ours. Furthermore, it can be noted that the small vortex on the right is rapidly dissipated and supplanted by the left vortex which, although progressively weakened, continues to widen exerting a momentum reintroduction action also on the leeward side of the wake (where lateral advection is “positive”). However, the mechanisms generated by the dominant vortex involve not only re-energizing the wake but also, on the contrary, extending the velocity deficit on the wake windward side where the flow moves out of the wake (“negative” lateral advection) because of the rotation direction of the vortex. As a result, at $4D$ and $6D$ the residual velocity deficit, and therefore the wake, appear extensively shifted on the windward side while the wake leeward side and most of the region behind the turbine appear completely re-energized. Figure 6 shows a completely different evolution of the wake in case of high-solidity camber-in blades. At $1D$ and $2.5D$ at the top of the wake a pair of counter-rotating small vortices can be seen, which origin is attributable to the tip vortices generated

during the downwind passage of the blades. A third small vortex is visible further to the right as a consequence of tip vortices generated in the second half of upwind, as already revealed by Fig. 4f. These vortices are smaller and much weaker than in case of camber-out profile so their momentum replenishment action is minor and only limited to the lateral advection visible at the wake windward side and to the upper-leeward corner, where freestream is entering into the wake. It should be observed that the rotation direction of the vortex pair generated during downwind implies “negative” vertical advection (i.e., the flow is outgoing the wake). Moreover, “negative” lateral advection is observable at the wake leeward side, coherently with the rotation direction of tip vortices generated during the second half of upwind, and, as a result, the wake appears slightly deviated on the right. Unlike the case of camber-out profile, these vortices are dissipated very quickly, so much so that further downstream than $2.5D$ no trace of them is seen anymore. Most of the recovery process takes place further ahead, at $4D$ and $6D$, where flows entering the wake can be seen from all directions; however, these motions instead to being correlated to tip vortices are due to the natural collapse of the wake as it is characterized by lower pressure than the high-momentum flow that surrounds it.

Comparing the streamwise velocity deficit at $6D$ for the cases with camber-out and camber-in profiles (Fig. 8) it is evident that the latter entail a much slower wake recovery. One more detail is worth observing, regarding the occurrence of negative streamwise velocities in the wake center in case of camber-in profile and high solidity. This is due to the wide recirculating region visible in Fig. 5. Negative streamwise velocities in CFT wakes were also noticed in experimental

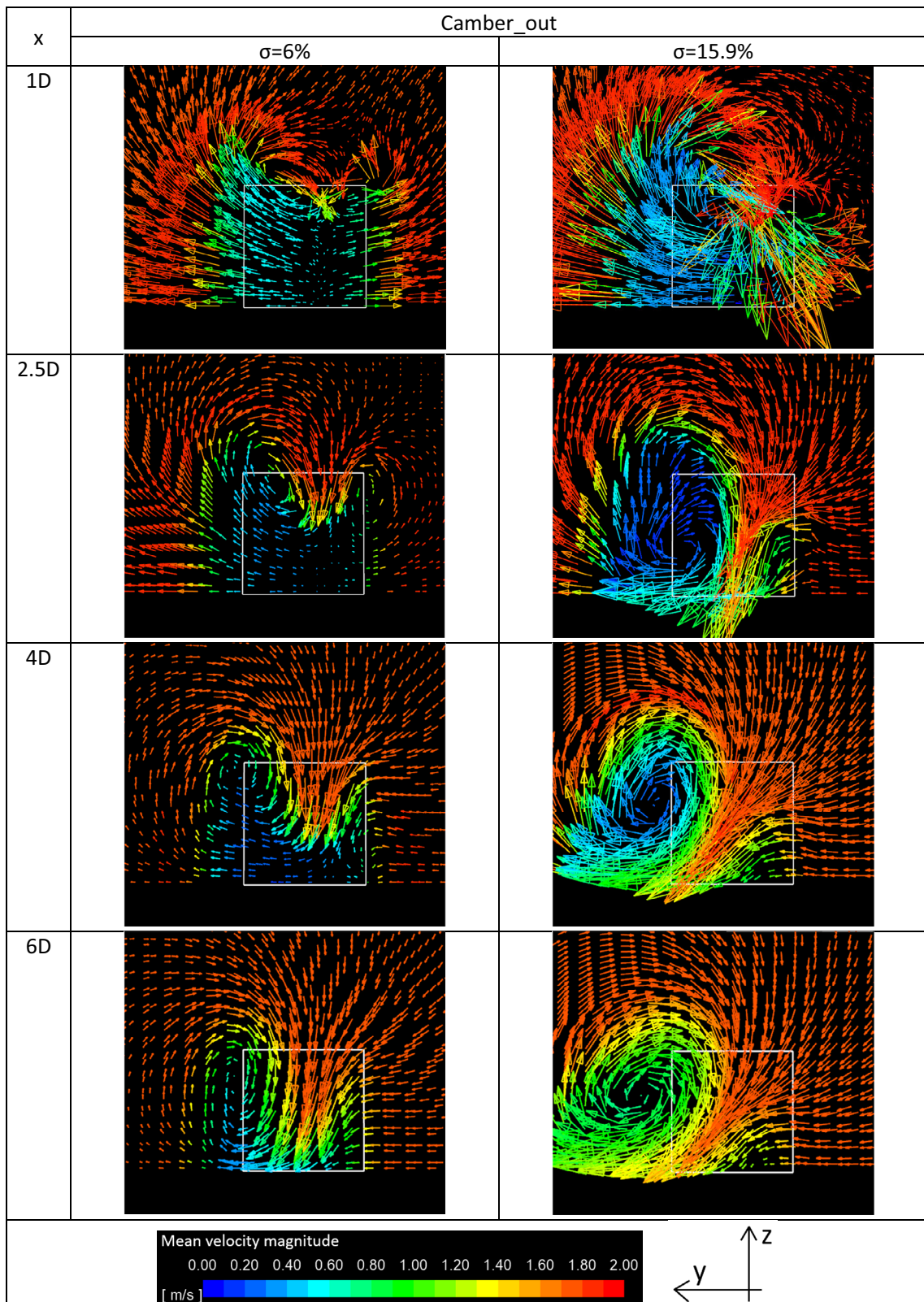


Fig. 6 Time-averaged crosswise velocity vectors in transversal planes at different positions downstream of the camber_out turbines ($x = 1D, 2.5D, 4D, 6D$); the white frame indicates the size of the turbine frontal area; colormap based on the mean velocity magnitude

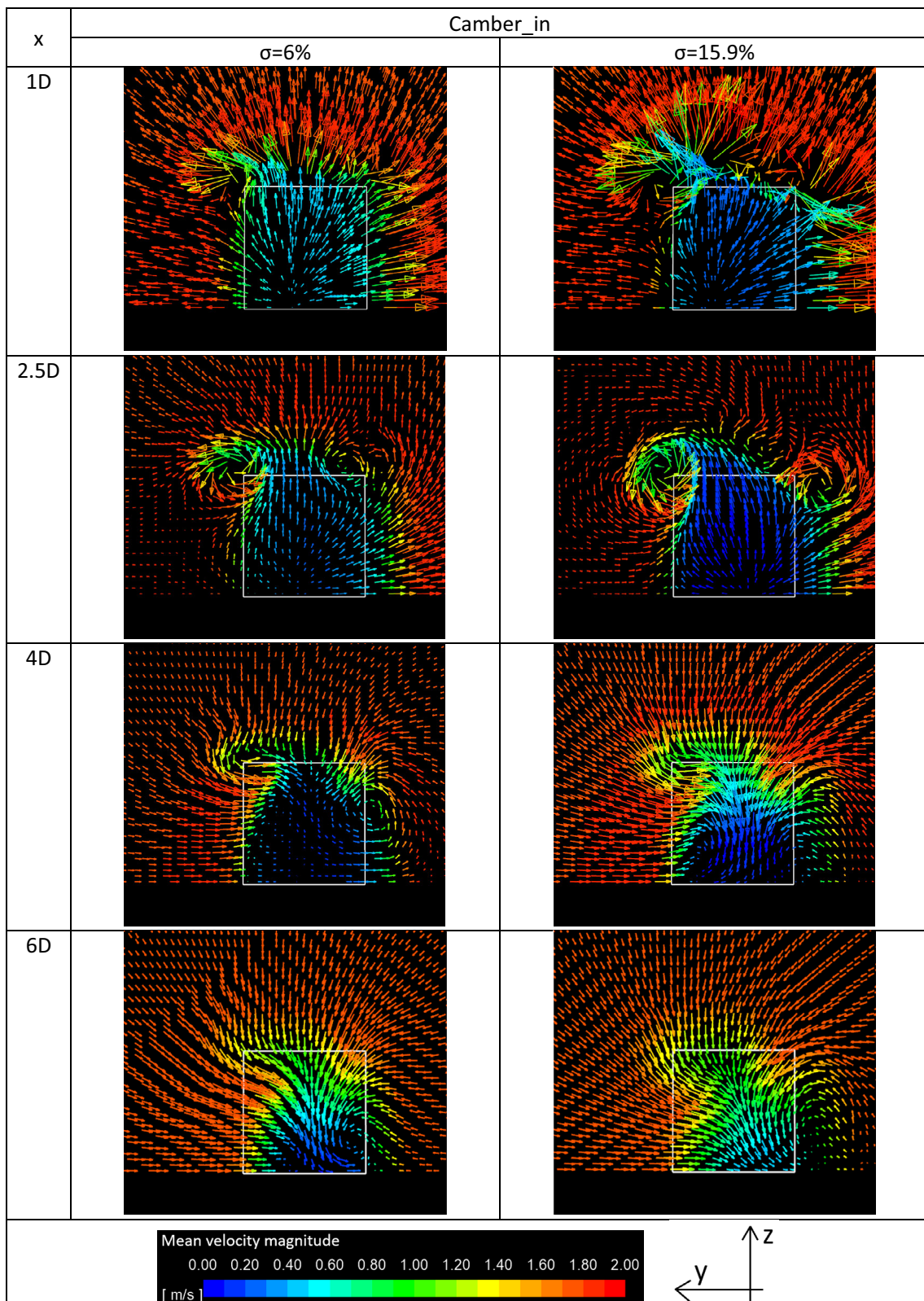


Fig. 7 Time-averaged crosswise velocity vectors in transversal planes at different positions downstream of the camber_in turbines ($x = 1D, 2.5D, 4D, 6D$); the white frame indicates the size of the turbine frontal area; colormap based on the mean velocity magnitude

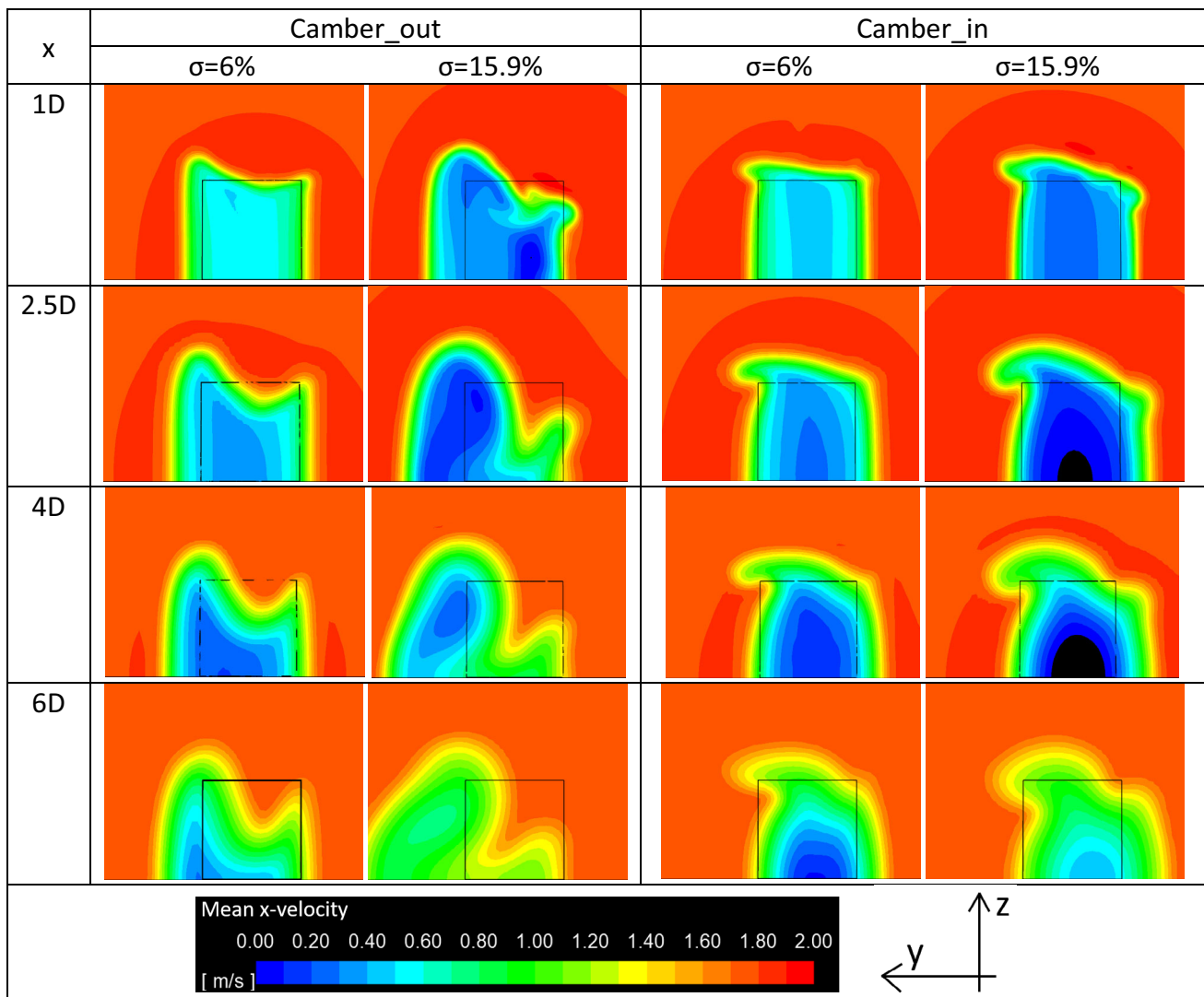


Fig. 8 Contours of the time-averaged streamwise velocity in transversal planes at different positions downstream of the four turbines ($x = 1D, 2.5D, 4D, 6D$); the black frame indicates the size of the turbine frontal area

studies (Araya et al. 2017; Brownstein et al. 2019; Parker and Leftwich 2016; Rolin and Porté-Agel 2015) and also in other numerical works (Chatelain et al. 2017; Hezaveh et al. 2017).

In case of low solidity, the wake evolution for camber-out and camber-in blades is qualitatively similar to the respective high-solidity cases, as depicted in Figs. 6, 7, 8, but the momentum recovery is slower and less complete. Indeed, at 6D it can be seen that the residual deficit of momentum is greater for both the low-solidity turbines in comparison to the high-solidity ones. The reason could be a smaller intensity of blade tip vortices.

It is also interesting a qualitative comparison on the contribution of turbulence to the mixing process and therefore energy recovery of the wake for the four turbines examined. To this end, Fig. 9 shows the contours of the Root Mean

Square (RMS) of the x, y and z components of the velocity on planes that are distant from the rotation axis 1, 2, 3, 4, 5 and 6D. Each plane has been cut out with the iso-contour of U corresponding to the freestream velocity, so as to highlight only the wake region (i.e. where $U < U_0$). The RMS of the velocity components represent the turbulent fluctuations calculated during the last 2 revolutions:

$$RMS_U = \sqrt{\frac{1}{N_{ts}} \sum_{i=1}^{N_{ts}} (U_i - \bar{U})^2} = \sqrt{\frac{1}{N_{ts}} \sum_{i=1}^{N_{ts}} (U'_i U'_i)}$$

$$RMS_V = \sqrt{\frac{1}{N_{ts}} \sum_{i=1}^{N_{ts}} (V_i - \bar{V})^2} = \sqrt{\frac{1}{N_{ts}} \sum_{i=1}^{N_{ts}} (V'_i V'_i)}$$

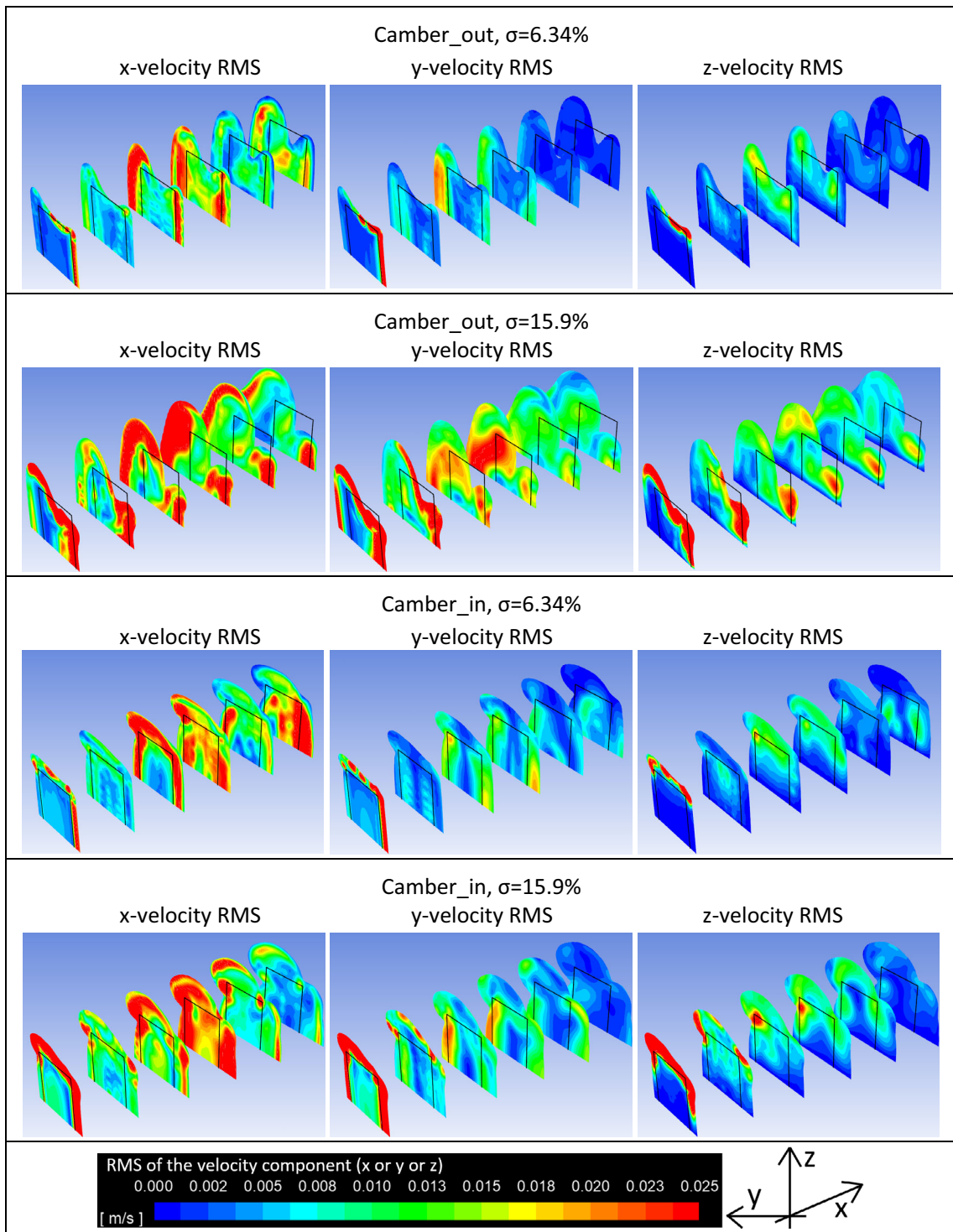


Fig. 9 RMS contours of x , y and z velocity components in transversal planes at different positions downstream of the turbine ($x = 1D, 2D, 3D, 4D, 5D, 6D$); each plane is cut by the x -velocity iso-contour $U =$

U_0 (meaning that only the wake region is shown, i.e. where $U < U_0$); the black frame indicates the size of the turbine frontal area

$$\text{RMS}_W = \sqrt{\frac{1}{N_{ts}} \sum_{i=1}^{N_{ts}} (W_i - \bar{W})^2} = \sqrt{\frac{1}{N_{ts}} \sum_{i=1}^{N_{ts}} (W'_i W'_i)}$$

where N_{ts} is the number of time-steps. Some general findings can be remarked: the RMS are much more prominent in the case of high solidity than in the case of low solidity, and in the case of camber-out blade than in the case of camber-in blade; the greatest RMSs occur in the medium wake (the maximum values at about 4D downstream of the turbine axis); the RMS of the x component of the velocity are greater than those of the y and z components; significant RMS are observed at the periphery of the wake, where high shear stresses are expected due to the high velocity gradients induced by the high-momentum flow enveloping the wake). The last result listed is in line with the literature (Rolin and Porté-Agel 2018), which has highlighted that the highest turbulent transport values are localized at the boundaries of the wake.

It is also interesting to note that in the case of high-solidity camber-out blades the RMS of the y and z velocities are very large.

The overall effect of turbulence on the wake mixing mechanisms are illustrated in Fig. 10, showing the contours of the turbulent kinetic energy (k) on the same crosswise planes. The black frame indicates the size of the turbine frontal area. The two high-solidity turbines are characterized by very large k values compared to the two low-solidity turbines, regardless of the blade shape. If we compare Figs. 8 and 10 we could deduce that in the medium wake a relationship exists between a strong turbulence extended to the heart of the wake and the obtaining of a significant degree of mixing and homogenization of the streamwise velocity, although starting from intense velocity deficits in the near wake.

Figures 6, 7, 8, 9 showed that the extension of the wake (i.e. the velocity deficit with respect to U_0), its shape and the position of its center of gravity differ considerably from those of the projection of the frontal area of the turbine (i.e., the white / black frame). These evidences prove the correctness of the choice made to assume the real area of the wake (and not the area delimited by the rectangular frame) to carry out the spatial averages relative to the terms that contribute to the recovery of the wake according to the momentum budget method.

3.3 Wake development and recovery: momentum budget computations

Before analyzing the main terms that appear in the momentum budget equation, it is useful to take a look at the evolution of the variables that mostly characterize the wake, i.e. velocity components, wake transversal extension, velocity uniformity on the transverse planes, power flow in the

wake. These characteristics, shown in Fig. 11, were averaged in space (on the clipping of the plane delimiting the wake) with the obvious exception of the extent of the wake, and in time.

The diagram of the velocity components (Fig. 11a) shows that U , V and W in general are greater for the cases of high solidity, and for the cases of camber-out blades with respect to those camber-in. However, V and W components are almost negligible compared to U and, as also confirmed by the velocity deficit diagram (Fig. 11b) in which it can be seen that the velocity magnitude deficit is almost coincident with the streamwise velocity deficit. The high-solidity case with camber-out blades is an exception, for which V and W are also significant.

Moving towards increasing values of x/D it can be seen (Fig. 11c) that the wake gradually expands and that at the same time the non-uniformity of U , defined as the standard deviation with respect to space:

$$\text{Spatial stand. deviation of } U : \sqrt{\sum_{i=1}^{N_f} (\bar{U}_i - \langle \bar{U} \rangle)^2 / N_f}$$

decreases (N_f is the number of cell faces on the wake crosswise section). Since low values of standard deviation mean high uniformity of the variable, it can be observed that the wakes of turbines with high solidity and camber-out blades homogenize relatively quickly. The last diagram (Fig. 11d) shows the energy flow. It is not a trivial result that the best values occur in the case of high solidity and camber-out blades due to the cubic dependence of the kinetic power on the velocity, for this to happen despite a greater degree of uniformity of U , it is also necessary that the spatial-averaged U is significantly greater than in the other cases. Which is exactly what happens.

On the right hand of Eq. 2 there is the gradient of the streamwise velocity along x -axis, then a positive value means that the x -momentum is recovering while a negative value means that it is decreasing further. A positive value for a term on the right hand means that it is contributing to the wake recovery, for instance, a positive y advection (or lateral advection) indicates that flow moving along the y -axis is (on average) entering the wake. The left-hand side of Eq. 2 (wake recovery rate) is compared for the four turbines in Fig. 12a: wake recovery appears delayed for camber-in profile; low solidity implies slower recovery for both the profiles. The diagrams in Fig. 12b and c describe the streamwise evolution for advection terms at the right hand of Eq. 2. It can be observed that: for camber-out profile, z advection is positive already starting from the near wake, while for camber-in profile both the advection terms are negative in the near wake and became positive later, when the wake collapse. It is not

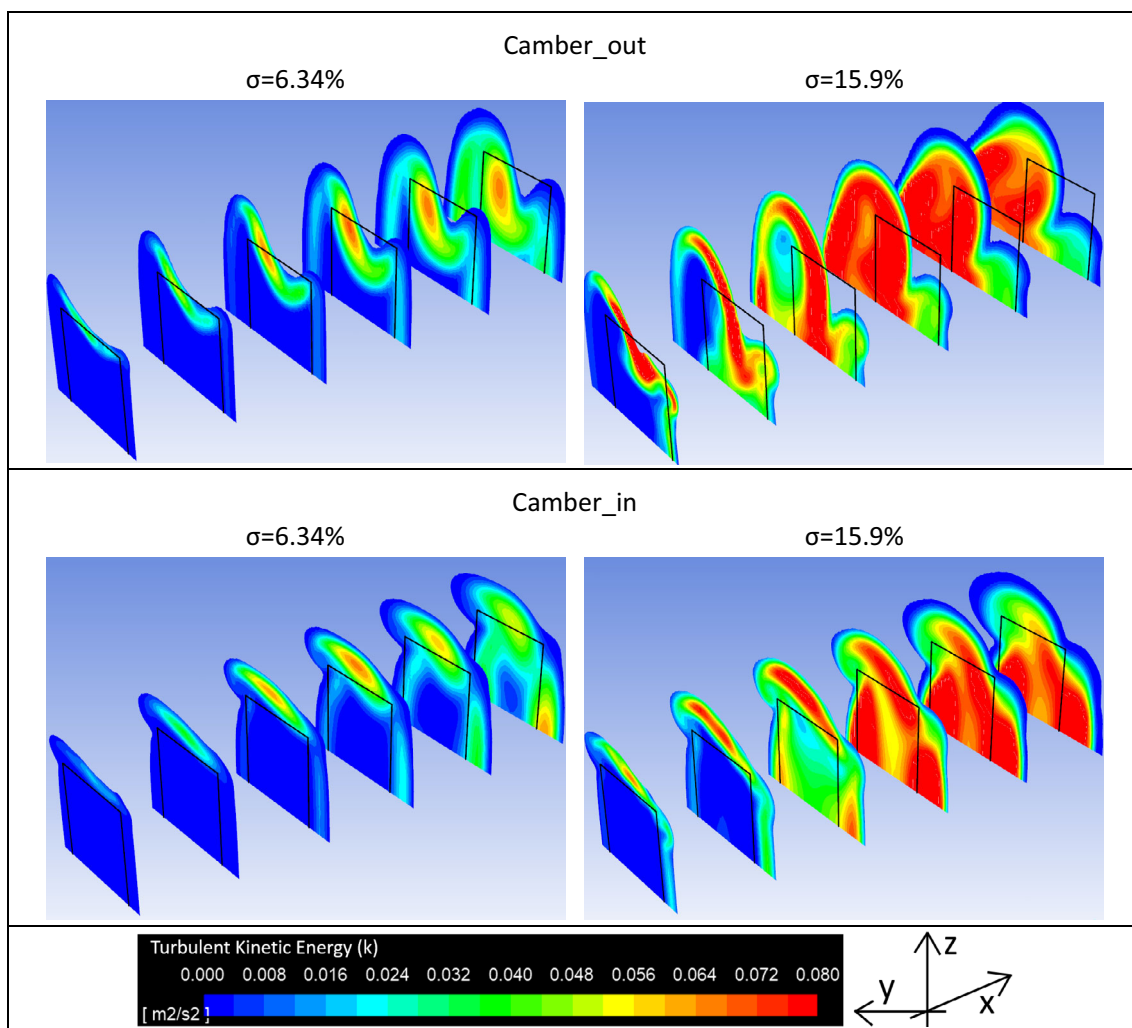


Fig. 10 Contours of the turbulent kinetic energy (k) in transversal planes at different positions downstream of the turbine ($x = 1D, 2D, 3D, 4D,$

$5D, 6D$); each plane is cut by the x -velocity iso-contour $U = U_0$ (meaning that only the wake region is shown, i.e. where $U < U_0$); the black frame indicates the size of the turbine frontal area

surprising that, in case of high solidity and camber-out profile, after $3D$ y -advection seems to exceed z advection this happens as the main flow entering the wake becomes oblique, that is, it has both z and y components, as clearly visible in Fig. 6 at $x = 4D$ and $6D$.

As already clarified, it was not possible to measure the turbulent transport terms that appear in Eq. 2. However, to get an idea of the contribution of turbulence in dependence on the solidity and shape of the blade, the values (space-averaged, as done for the terms of Eq. 2) of the velocity RMSs and k were calculated, and their streamwise evolution is shown in Fig. 12e and f. In the diagrams, the RMSs were dimensionless by dividing them by U_0 , while k was divided by the square of U_0 . The values of k are instantaneous (therefore not averaged over time).

Figure 12e shows that turbulent fluctuations (RMS) of the velocity components are significant, and therefore can contribute to the energy recovery, only in case of high solidity, and their amount appear important starting from $3.5D$ for both the camber-out and the camber-in profiles. The very high values of the velocity RMS at $x/D = 1$ should not be misleading, indeed they are due to the fact that the very close passage of the blade implies large variations in local flow velocity with the blade angular position θ , while increasing the distance from the turbine the effects of the blade phase are less and less relevant. Figure 12f indicates a remarkable occurrence of turbulent kinetic energy in case of high solidity, especially from the medium wake (see that at $4D$ it is higher than at $2.5D$). The result that turbulent mixing is a “late” phenomenon is in line with the literature. It is also interesting to note that high solidity implies much greater k than low

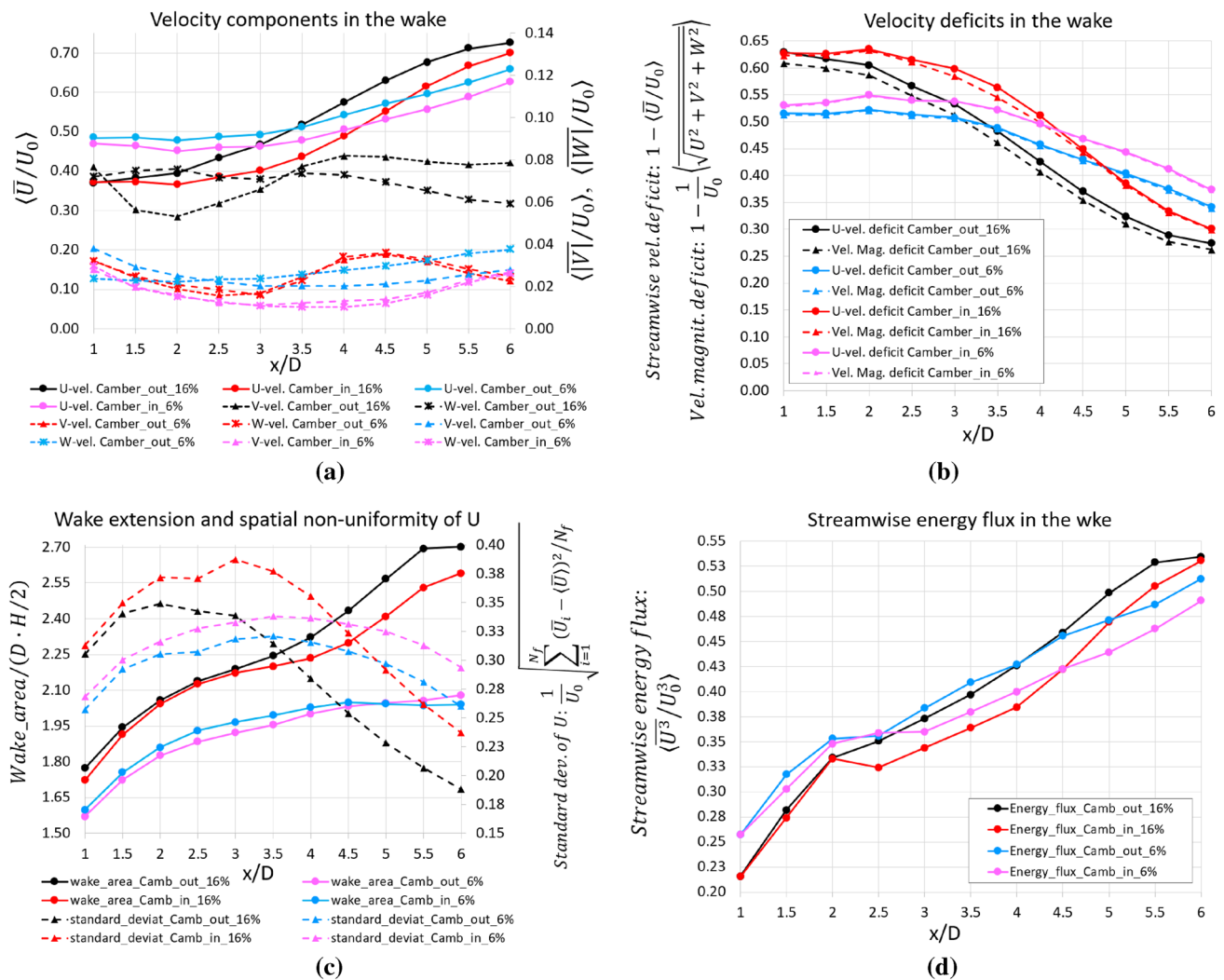


Fig. 11 Some characteristics of the wake at different positions downstream of the turbine axis: **a** U , V and W velocity components; **b** deficit of the streamwise (U) velocity and of the velocity magnitude; **c** wake

area, and spatial standard deviation of U . The values shown in **a**, **b** and **d** are averaged in space (on the clipping of the plane delimiting the wake) and in time (on the last 2 revs.)

solidity and therefore higher aptitude to the wake recovery. The same is true for the camber-out blades compared to the camber-in blades.

Given these results, and considering the interesting potential in terms of high starting torque (Rainbird et al. 2015), especially if a variable pitch is adopted (Kirke and Lazauskas 1991; Coiro et al. 2005; Chougule and Nielsen 2014; Zhang et al. 2015), one could conclude that camber-out profiles could be the most suitable choice also for farms thanks to their wake recovery properties.

4 Conclusions

Blade tip vortices can be considered the main precursors of the large-scale flow structures found in the wake of CFTs.

The main findings of this analysis on the origin and characteristics of tip vortices and on the wake recovery mechanisms, in relation to the turbine geometry (turbine solidity and cambering direction), are the following.

- Since the strength of the blade tip vortices depends on the pressure difference between the two sides of the blade, it is very high during upwind for camber-out profiles while it is more smoothly distributed between upwind and downwind for camber-in profiles.
- The x -vorticity of the blade tip vortices determines the rotation direction of the vortices in the wake; since its sign only depends on the blade revolution quadrant, the sign of the wake vortices is established by the quadrants where strong tip vortices are generated.

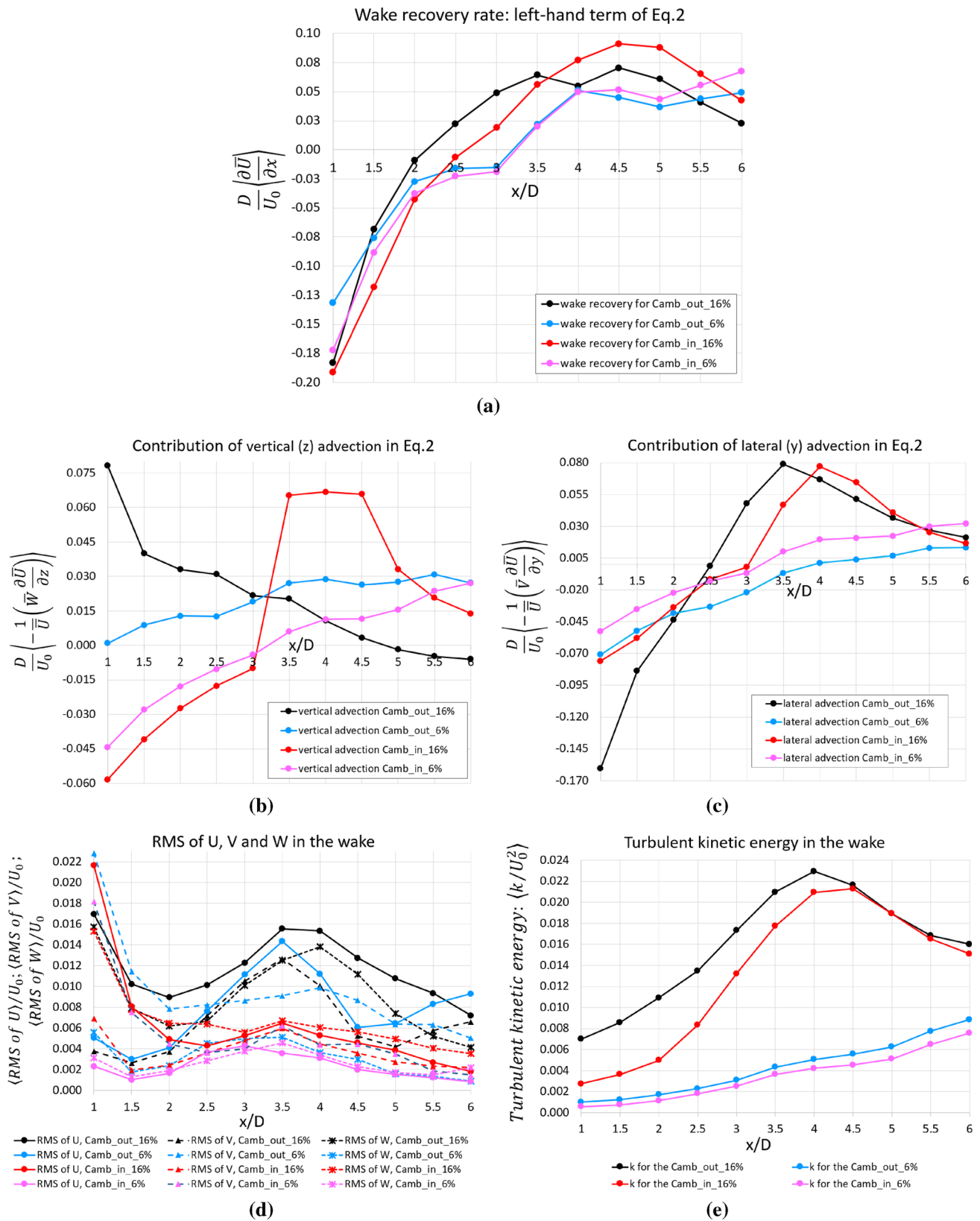


Fig. 12 Wake recovery rate and some main players in the energy recovery process at different positions downstream of the turbine axis: **a** wake recovery rate (left-hand term in Eq. 2); **b** vertical advection (see Eq. 2); **c** lateral advection (see Eq. 2); **d** RMS of U , V and W ; **e** turbulent

kinetic energy. In all the diagrams the values are averaged in space (on the clipping of the plane delimiting the wake), and in time (on the last 2 revs.) with the exception of k (that are instantaneous values)

- Pairs of counter-rotating vortices occurs in the wake, which rotation direction depends on blade profile and it is such as to generate positive vertical advection for camber-out profiles, but negative vertical advection for camber-in profiles.
- The blade tip vortices of camber-out profiles are very effective in supporting wake recovery, being the vertical advection induced by tip vortices the main contribution to the momentum recovery.
- For camber-in profiles the strength of tip vortices is too small and their rotation direction is poorly effective to support the momentum recovery, that appears delayed and mainly governed by wake collapse and turbulent transport.
- Higher solidity implies much stronger tip vortices and therefore faster wake recovery.
- For both the profiles, turbulent transport is important in the case of high-solidity turbines, as evidenced by the turbulent kinetic energy and the velocity RMSs, which values appear maximum in the range $3.5D \div 4.5D$ downstream of the turbine axis.

Acknowledgements The author sincerely thanks Paola Lupi for having collaborated in the validation phase of the numerical model against the experimental data found in the literature.

Funding Open access funding provided by Università di Pisa within the CRUI-CARE Agreement. This research did not receive funding.

Declarations

Conflict of interest The author are not in conditions of conflict of interest with the research carried out and presented in this manuscript.

Open Access This article is licensed under a Creative Commons Attribution 4.0 International License, which permits use, sharing, adaptation, distribution and reproduction in any medium or format, as long as you give appropriate credit to the original author(s) and the source, provide a link to the Creative Commons licence, and indicate if changes were made. The images or other third party material in this article are included in the article's Creative Commons licence, unless indicated otherwise in a credit line to the material. If material is not included in the article's Creative Commons licence and your intended use is not permitted by statutory regulation or exceeds the permitted use, you will need to obtain permission directly from the copyright holder. To view a copy of this licence, visit <http://creativecommons.org/licenses/by/4.0/>.

References

Ahmadi-Baloutaki M, Carriveau R, Tinga DS (2016) A wind tunnel study on the aerodynamic interaction of vertical axis wind turbines in array configurations. *Renew Energ* 96:904–913

- Araya DB, Colonius T, Dabiri JO (2017) Transition to bluff-body dynamics in the wake of vertical-axis wind turbines. *J Fluid Mech* 813:346–381
- Bachant P, Wosnik M (2015) Characterising the near-wake of a cross-flow turbine. *J Turbul* 16(4):392–410
- Balduzzi F, Bianchini A, Maleci R, Ferrara G, Ferrari L (2016) Critical issues in the CFD simulation of Darrieus wind turbines. *Renew Energy* 85:419–435
- Boudreau M, Dumas G (2017) Comparison of the wake recovery of the axial-flow and cross-flow turbine concepts. *J Wind Eng Ind Aerodyn* 165:137–152
- Brownstein ID, Wei NJ, Dabiri JO (2019) Aerodynamically interacting vertical-axis wind turbines: performance enhancement and three-dimensional flow. *Energies* 12:2724
- Chatelain P, Duponcheel M, Zeoli S, Buffin S, Caprace D-G, Winckelmans G, Bricteux L (2017) Investigation of the effect of inflow turbulence on vertical axis wind turbine wakes. *J Phys Conf Ser* 854:012011
- Chougule P, Nielsen S (2014) Overview and design of self-acting pitch control mechanism for vertical axis wind turbine using multi body simulation approach. *J Phys Conf* 524:012055
- Coiro DP, Nicolosi F, De Marco A, Melone S, Montella F (2005) Dynamic behavior of novel vertical axis Tidal current turbine: numerical and experimental investigations. In: Proc. of 15th Int. Offshore and Polar Engin. Conf. Seoul, Korea
- Dabiri JO (2011) Potential order-of-magnitude enhancement of wind farm power density via counter-rotating vertical-axis wind turbine arrays. *J Renew Sustain Energy* 3:43104
- Hau NR, Ma L, Ingham D, Pourkashanian M (2020) A critical analysis of the stall onset in vertical axis wind turbines. *J Wind Eng Ind Aerodyn* 204:104264
- Hezaveh SH, Bou-Zeid E, Lohry MW, Martinelli L (2017) Simulation and wake analysis of a single vertical axis wind turbine. *Wind Energy* 20(4):713–730
- Karimian S, Abdolahifar A (2020) Performance investigation of a new Darrieus vertical axis wind turbine. *Energy* 191:116551
- Kinzel M, Mulligan Q, Dabiri JO (2012) Energy exchange in an array of vertical-axis wind turbines. *J Turbul* 13:1–13
- Kirke BK, Lazauskas L (1991) Enhancing the performance of vertical axis wind turbine using a simple variable pitch system. *Wind Eng* 15(4):187–195
- Maître T, Amet E, Pellone C (2013) Modeling of the flow in a Darrieus water turbine: wall grid refinement analysis and comparison with experiments. *Renew Energy* 51:497–512
- Marsh P, Ranmuthugala D, Penesis I, Thomas G (2017) The influence of turbulence model and two and three-dimensional domain selection on the simulated performance characteristics of vertical axis tidal turbines. *Renew Energy* 105:106–116
- Menter FR (1994) Two-equation eddy-viscosity turbulence models for engineering applications. *AIAA J* 32:1598–1605
- Ouro P, Runge S, Luo Q, Stoesser T (2019) Three-dimensionality of the wake recovery behind a vertical axis turbine. *Renew Energy* 133:1066–1077
- Parker CM, Leftwich MC (2016) The effect of tip speed ratio on a vertical axis wind turbine at high Reynolds numbers. *Exp Fluids* 57(5):74
- Posa A (2020) Dependence of the wake recovery downstream of a Vertical Axis Wind Turbine on its dynamic solidity. *J Wind Eng Ind Aerodyn* 202:104212
- Posa A, Broglia R (2021) Momentum recovery downstream of an axial-flow hydrokinetic turbine. *Renew Energy* 170:1275–1291
- Qin N, Danao LA, Howell R (2012) A numerical study of blade thickness and camber effects on vertical axis wind turbines. *Proc Inst Mech Eng a: J Power Energy* 226(7):867–881
- Rainbird JM, Bianchini A, Balduzzi F, Peiró J, Graham JMR, Ferrara G, Ferrari L (2015) On the influence of virtual camber effect on

- airfoil polars for use in simulations of Darrieus wind turbines. *Energy Convers Manag* 106:373–384
- Rezaeiha A, Montazeri H, Blocken B (2019) On the accuracy of turbulence models for CFD simulations of vertical axis wind turbines. *Energy* 180:838–857
- Rolin V, Porté-Agel F (2015) Wind-tunnel study of the wake behind a vertical axis wind turbine in a boundary layer flow using stereoscopic particle image velocimetry. *J Phys Conf Ser* 625:012012
- Rolin VF-C, Porté-Agel F (2018) Experimental investigation of vertical-axis wind-turbine wakes in boundary layer flow. *Renew Energy* 118:1–13
- Ryan KJ, Coletti F, Elkins CJ, Dabiri JO, Eaton JK (2016) Three-dimensional flow field around and downstream of a subscale model rotating vertical axis wind turbine. *Exp Fluids* 57:38
- Su H, Meng H, Qu T, Lei L (2021) Wind tunnel experiment on the influence of array configuration on the power performance of vertical axis wind turbines. *Energy Convers Manag* 241:114299
- Vergaerde A, De Troyer T, Muggiasca S, Bayati I, Belloli M, Kluczewska-Bordier J, Parneix N, Silvert S, Runacres MC (2020) Experimental characterisation of the wake behind paired vertical-axis wind turbines. *J Wind Eng Ind Aerodyn* 206:104353
- Villeneuve T, Dumas G (2021) Impact of some design considerations on the wake recovery of vertical-axis turbines. *Renew Energy* 180:1419–1438
- Villeneuve T, Boudreau M, Dumas G (2020) Improving the efficiency and the wake recovery rate of vertical-axis turbines using detached end-plates. *Renew Energy* 150:31–45
- Wei N, Brownstein ID, Cardona JL, Howland MF, Dabiri JO (2021) Near-wake structure of full-scale vertical-axis wind turbines. *J Fluid Mech* 914:A17
- Wilcox DC (2008) Formulation of the $k-\omega$ turbulence model revisited. *AIAA J* 46:2823–2838
- Zanforlin S (2018) Advantages of vertical axis tidal turbines set in close proximity: a comparative CFD investigation in the English Channel. *Ocean Eng* 156:358–372
- Zanforlin S, Deluca S (2018) Effects of the Reynolds number and the tip losses on the optimal aspect ratio of straight-bladed Vertical Axis Wind Turbines. *Energy* 148:179–195
- Zanforlin S, Nishino T (2016) Fluid dynamic mechanisms of enhanced power generation by closely spaced vertical axis wind turbines. *Renew Energy* 99:1213–1226
- Zhang LX, Pei Y, Liang YB, Zhang FY, Wang Y, Meng JJ, Wang HR (2015) Design and implementation of straight-bladed vertical Axis wind turbine with collective pitch control. In: *Proceedings of the 2015 IEEE Int. Conf. on Mechatronics and Automation*, Beijing, China, pp 2–5

Publisher's Note Springer Nature remains neutral with regard to jurisdictional claims in published maps and institutional affiliations.